





Injectable supramolecular hydrogel co-loading abemaciclib/NLG919 for neoadjuvant immunotherapy of triple-negative breast cancer

Received: 15 November 2023

Accepted: 4 January 2025

Published online: 15 January 2025

 Check for updates

Binyu Zhu^{1,2,10}, Ying Cai^{1,2,3,10}, Lingli Zhou⁴, Lei Zhao⁵, Jiameng Chen^{1,2}, Xiaoting Shan^{1,2}, Xujie Sun^{1,2}, Qian You⁶, Xiang Gong^{1,7}, Wen Zhang^{1,7}, Helen He Zhu⁶, Pengcheng Zhang⁸   & Yaping Li^{1,2,3,4,9}  

The efficacy of cancer immunotherapy relies on a sufficient amount of functional immune cells. Triple-negative breast cancer lacks enough immune cell infiltration, and adjuvant therapy is necessary to prime anti-tumor immunity. However, the improvement in efficacy is unsatisfactory with concern about inducing systemic immunotoxicity. Herein, we create an abemaciclib-loaded supramolecular peptide hydrogel formed by peptide-drug amphiphiles for neoadjuvant immunotherapy of triple-negative breast cancer, where the amphiphile is a conjugate of a β -sheet-forming peptide with 1-cyclohexyl-2-(5H-imidazo[5,1-a]isoindol-5-yl)ethanol (NLG919), an inhibitor of indoleamine 2,3-dioxygenase 1. The hydrogel can be injected into the tumor site and retained for at least one week for the sustained release of both abemaciclib and NLG919. The abemaciclib is able to induce immunogenic cell death of cancer cells and increase interleukin-2 secretion by cytotoxic T lymphocytes. Abemaciclib adversely upregulates indoleamine 2,3-dioxygenase 1, whose kynurenine production activity is inhibited by NLG919. The neoadjuvant immunotherapy reduces tumor recurrence and pulmonary metastasis and prolongs the survival of animals. This hydrogel provides a potential platform for neoadjuvant immunotherapy of triple-negative breast cancer with reduced toxicity compared with free abemaciclib.

Cancer immunotherapy has revolutionized the field of cancer therapy. However, immunotherapy alone has moderate efficacy in many advanced cancers such as triple-negative breast cancer (TNBC)^{1–4}. TNBC is considered the subtype that can benefit the most from immunotherapy among breast cancer^{5,6} because it is the most immunogenic subtype^{7–9} with a high propensity to generate neoantigens¹⁰ and high immune signature scores. Therefore, the low response rate of TNBC to immunotherapy may be associated with the relatively low infiltration of cytotoxic T lymphocytes (CTLs) compared with other

types of cancers such as melanoma¹¹. Indeed, TNBC with a higher level of T lymphocytes typically predicts a better prognosis^{12–15}. To address this issue, the combination use of chemotherapy and immunotherapy has been explored, as many chemotherapeutic agents can directly kill cancer cells and subsequently prime anti-tumor immunity by triggering the release of immunostimulatory molecules and inhibiting immunosuppressive cells^{16–19}.

Neoadjuvant therapy (administered before surgical resection) has recently received increasing attention. Neoadjuvant chemotherapy

helps identify effective drugs that can shrink the primary tumor for further lumpectomy and guide further adjuvant therapy against metastatic loci^{20–22}. Particularly, neoadjuvant chemotherapy can induce anti-tumor immunity and restore immune surveillance in breast cancer patients^{23,24}. For instance, the combined use of Abraxane and immune checkpoint inhibitor as a neoadjuvant therapy outperformed Abraxane monotherapy as the first-line treatment for advanced TNBC^{18,25–27}. Although treatment prolonged the median progression-free survival of the intention-to-treat population with advanced TNBC based on the IMpassion 130 trial, no statistically significant benefit in the final overall survival analysis was observed in this population²⁶. In addition, systemic chemotherapy usually impairs immune cells, leading to neutropenia and lymphopenia^{28–30}. Patients with metastatic TNBC who have undergone extensive chemotherapy usually show a lower overall response rate to subsequent pembrolizumab treatment than untreated patients³¹, highlighting the essential role of the functional immune system during TNBC immunotherapy. Therefore, an effective treatment for TNBC with low immunotoxicity is still of urgent need.

Molecular targeted therapy has emerged as a promising treatment for cancer because of its less severe side effects compared with cytotoxic agents, as these targets are highly expressed or activated in cancer cells^{32,33}. Many types of cancer, including breast cancer, overexpress or hyperactivate cyclin-dependent kinases 4 and 6 (CDK4/6), and several CDK4/6 inhibitors have been approved for cancer therapy³⁴. Among these inhibitors, Abemaciclib (Abe) exhibits the most potent CDK4/6 inhibitory activity^{35,36}, and has been approved for advanced or metastatic hormone receptor-positive breast cancer^{37,38}. Abe is also effective in priming anti-tumor immunity with less severe myelosuppression, although prolonged Abe exposure may impair lymphocyte proliferation^{39,40}. Given its ability to elicit immune priming activity, Abe is currently being tested in patients with surgically resectable chemotherapy-resistant TNBC (NCT03979508). Nevertheless, Abe, like most anti-tumor drugs, may upregulate the intratumoral expression of indoleamine 2,3-dioxygenase 1 (IDO-1), which converts tryptophan (Trp) into kynurenine (Kyn), thus creating an immunosuppressive tumor microenvironment by activating regulatory T cells (T_{Reg})^{41–43}. The prolonged depletion of Kyn using PEGylated Kynureninase reverses the immunosuppressive microenvironment⁴⁴. However, the IDO-1 inhibitor failed in the phase I/II trial, largely because of its transient tumor exposure^{45,46}. Therefore, a local and sustained delivery of Abe and IDO-1 inhibitors, which may exhibit synergistic efficacy against TNBC, is required.

Hydrogel is an ideal platform for local drug delivery⁴⁷. Recently, considerable efforts have been devoted to the development of injectable hydrogels that can be delivered easily through local injection. Based on the mechanism of gelation, stimuli-triggered in situ hydrogel and shear-thinning hydrogel are the two most common types of injectable hydrogels^{48,49}. An emerging type of injectable hydrogel is the supramolecular peptide hydrogel, in which nanofibers self-assembled from peptide-drug/lipid conjugates entangle to form a macroscale network^{50–54}. This type of one-component hydrogel has a high drug-loading capacity and elicits linear and sustainable drug release, which is directly associated with the gelation behavior^{55,56}. The hydrogel can also serve as a reservoir for additional small hydrophilic and hydrophobic molecules^{50,57}, biomacromolecules such as antibodies⁵⁸, and nanoparticles^{29,56}. Moreover, Abe suffers from rapid clearance⁵⁹, which can be addressed by encapsulating the drug within the hydrogel.

In this work, we report an injectable supramolecular hydrogel of Abe-loaded peptide-1-cyclohexyl-2-(5H-imidazo[5,1-a]isoindol-5-yl) ethanol (NLG919) nanofibers (Abe-NF(g)) for neoadjuvant immunotherapy of TNBC since TNBC is the most immunogenic subtype of breast cancer with an unsatisfactory response to immunotherapy mainly due to limited active CTL infiltration. NLG919 is conjugated to

the cysteine residue of a β -sheet forming peptide (Cysteine-Glycine-Valine-Valine-Glutamine-Glutamine-Histidine-Lysine-Aspartate, CGVVQHKD) through a disulfide bond to obtain the prodrug (NLG-HKD). The GVVQQ segments help form interpeptidic hydrogen bonding, while the HKD segments provide hydrophilic headgroups that facilitate the formation of hydrogels at physiological pH⁵⁴. NLG-HKD can self-assemble into nanofibers to further encapsulate Abe within the hydrophobic cores formed by NLG919, and the Abe-loaded nanofibers will entangle with each other to form Abe-NF(g) (Fig. 1a). The hydrogel is tested on a murine 4T1 tumor model because it recapitulates human TNBC according to a recent multi-omics analysis⁶⁰ with considerable expression of CDK4/6 and IDO-1. After local injection into the tumor site, Abe-NF(g) remains as a drug reservoir for the sustained release of Abe and NLG919 (Fig. 1b). Abe is expected to induce immunogenic cell death (ICD) of tumor cells, enhance the maturation of dendritic cells (DCs), and induce the differentiation of monocytes toward classically activated macrophages (M1). NLG919 is expected to be released from NLG-HKD after cellular entry and to inhibit IDO-1-mediated Kyn production and T_{Reg}, thereby relieving the immunosuppressive microenvironment. The two drugs in Abe-NF(g) function synergistically to improve the infiltration and activity of CD8⁺ T cells for effective immunotherapy of TNBC.

Results

Preparation and characterization of the Abe-NF(g)

To prepare the building block of the injectable supramolecular prodrug hydrogel, we first reacted the hydroxyl group of NLG919 with the carboxyl group of the bifunctional linker, 4-(Pyridin-2-yl)disulfanyl) butanoic acid (BuSS-Pyr), to obtain NLG919-4-(Pyridin-2-yl)disulfanyl) butanoic acid (NLG-Pyr) (Supplementary Fig. 1). NLG-Pyr was then reacted with the thiol group of a β -sheet forming peptide CGVVQHKD (Supplementary Fig. 2) to give NLG-HKD (Fig. 2a and Supplementary Fig. 3), which could be efficiently converted back into NLG919 (> 90% conversion within 24 h) in the presence of glutathione (GSH, 10 mM in phosphate-buffered saline (PBS), pH 7) (Fig. 2b). Further analysis showed that NLG-HKD would self-assemble in aqueous solution with a critical micelle concentration (CMC) of approximately 0.4 μ M (Fig. 2c and Supplementary Fig. 4). Cryo-transmission electron microscopy (cryo-TEM) revealed that NLG-HKD self-assembled into prodrug nanofibers (NF) with diameters of around 9 nm (Fig. 2d).

We then explored the ability of NF to encapsulate Abe using a co-assembly strategy. Abe could be efficiently entrapped within the prodrug nanofibers (encapsulation efficiency at $92.1 \pm 2.9\%$) to give Abe-loaded NFs (Abe-NFs) with a drug loading capacity at $3.1 \pm 0.1\%$. Cryo-TEM analysis revealed that Abe encapsulation had no significant influence on the self-assembly of NLG-HKD, with similar shapes and diameters recorded under the tested conditions (Fig. 2e and Supplementary Fig. 5). At neutral but not acidic pH, the Abe-NFs (> 7.5 mM) further entangled with each other to form a macroscopic hydrogel (Abe-NF(g)) (Fig. 2e, f and Supplementary Fig. 6). The formation of Abe-NF(g) (15 mM in NLG-HKD, pH 7) was evidenced by a higher storage modulus (G') than the loss modulus (G'') (Fig. 2f). Addition of salts or application of shear force (injection through 27G needle) 2 min before assessment led to no significant change in G' and G'' (Fig. 2g), which was further confirmed by an instant recovery of hydrogel after injection (Supplementary Fig. 7), suggesting that the Abe-NF(g) was a fast recovery hydrogel. Abe-loaded C₁₆-HKD (C₁₆-CGVVQHKD) nanofiber was prepared and used as a control in the following experiments, which were of similar morphology and ζ -potential (about -35 mV) as Abe-NFs and could form hydrogel (Abe-CF(g)) under similar conditions (Fig. 2h and Supplementary Fig. 8). We then monitored drug release from Abe-NF(g) of different concentrations (30.0 mM, 15.0 mM, 7.5 mM, and 3.8 mM in NLG-HKD). A linear drug release in a period of 7 days was recorded on hydrogels of 30.0 mM and 15.0 mM, which was in sharp contrast with free Abe and hydrogels of lower

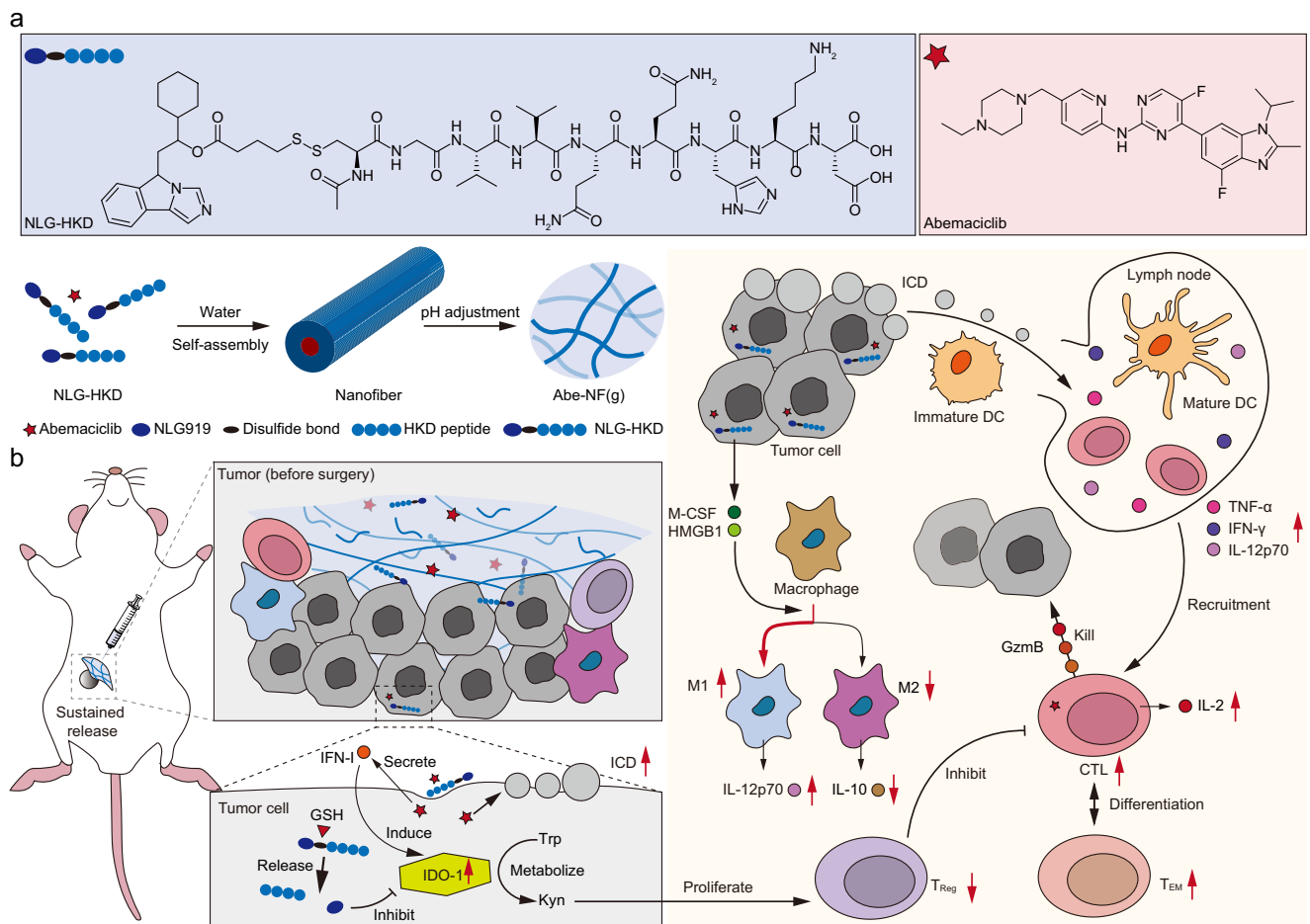


Fig. 1 | Schematic illustration of the design and mechanism of action of the injectable hydrogel as a neoadjuvant immunotherapy. a Design and preparation of the Abe-NF(g) supramolecular hydrogel. Prodrug NLG-HKD and Abe can co-assemble into Abe-loaded nanofibers, which further entangle to form the hydrogel. **b** The injectable hydrogel could be retained at the tumor site as a drug reservoir for sustained release of Abe and NLG919. The Abe could induce ICD of cancer cells and IL-2 secretion of CTLs, and thus promote DC maturation and M1 differentiation. NLG-HKD can be converted into NLG919 in the presence of intracellular GSH and the released NLG919 is able to inhibit the activity of IDO-1, the expression of which

may be upregulated by Abe, maintaining a low level of Kyn and T_{Reg} within the tumor. The two drugs exert a synergistic effect in improving CTL-mediated anti-tumor immunity and immune memory. ICD immunogenic cell death, Trp tryptophan, Kyn kynurenine, DC dendritic cell, T_{Reg} regulatory T cell, T_{EM} effector memory T cell, CTL cytotoxic T lymphocyte, IFN-1 type I interferon, IDO-1 indoleamine 2, 3-dioxygenase 1, IL-2 interleukin-2, GzmB granzyme B, TNF- α tumor necrosis factor- α , IFN- γ interferon- γ , IL-12p70 interleukin-12 p70, M-CSF macrophage colony-stimulating factor, HMGB1 high mobility group box 1, IL-10 interleukin-10, GSH glutathione, Abe abemaciclib.

concentrations (Fig. 2i and Supplementary Fig. 9). However, the hydrogel of 30.0 mM could not be injected through the 27 G needle due to its high viscosity (Supplementary Fig. 9). Therefore, the hydrogel of 15.0 mM was used for subsequent experiments. These results demonstrated that NLG-HKD could co-assemble with Abe into nanofibers, which further formed an injectable supramolecular hydrogel in a pH-dependent manner. Abe-NF(g) served as a reservoir for Abe, enabling its prolonged release, whose behavior was profoundly influenced by the concentration of the hydrogel.

The activity of Abe-NF in vitro

First, we tested the anti-tumor activity of Abe in vitro and found that free Abe and Abe-NFs showed comparable efficacy (Supplementary Fig. 10). Based on these results, we explored whether it was effective in inducing ICD. Quantitative analysis revealed that Abe-NFs, in comparison with PBS, increased the release of ATP by 5.2-fold (Fig. 3a). Both qualitative and quantitative assays showed that Abe-NFs increased the release of high mobility group box 1 (HMGB1) by 2.4-fold (Fig. 3b and Supplementary Fig. 11) and induced surface exposure of calreticulin (CRT) on 4T1 cells by ~30% (Fig. 3c and Supplementary Fig. 12). The efficacy of Abe-NFs was comparable to that of free Abe,

whereas the NFs did not induce ICD. In contrast, the same treatments had no significant activities on CDK4/6 knockout 4T1 cells (Supplementary Fig. 13). These results suggested that Abe-NFs could potentially prime anti-tumor immunity by inhibiting CDK4/6 of cancer cells.

Based on these findings, we explored the influence of Abe-NFs-treated cancer cells on either bone marrow-derived dendritic cells (BMDCs) or bone marrow-derived macrophages (BMDMs) using a coculture model (Fig. 3d). As expected, the proportion of matured DCs ($CD11c^+CD80^+CD86^+$) was increased from 13.5% (PBS group) to 21.7% and 27.4% by Abe- and Abe-NF-treated 4T1 cells, respectively, whereas NF alone showed no significant effect (Fig. 3e). In contrast, the pre-treated CDK4/6 knockout 4T1 cells ($4T1^{CDK4/6 KO}$) showed no activity in boosting DC maturation (Supplementary Fig. 13). Additionally, the number of M1 ($CD11b^+F4/80^+CD80^+$) was increased by approximately 34% by Abe-NF, while the same treatment reduced the number of alternatively activated macrophages (M2, $CD11b^+F4/80^+CD206^+$) by more than 20% (Fig. 3f). Since the total number of macrophages was not significantly altered by the treatments, Abe-containing treatments increased the M1-to-M2 ratio of BMDMs, probably because of the preferential induction of progenitor cells into M1 (Supplementary Fig. 14). Our previous study showed that macrophage colony-

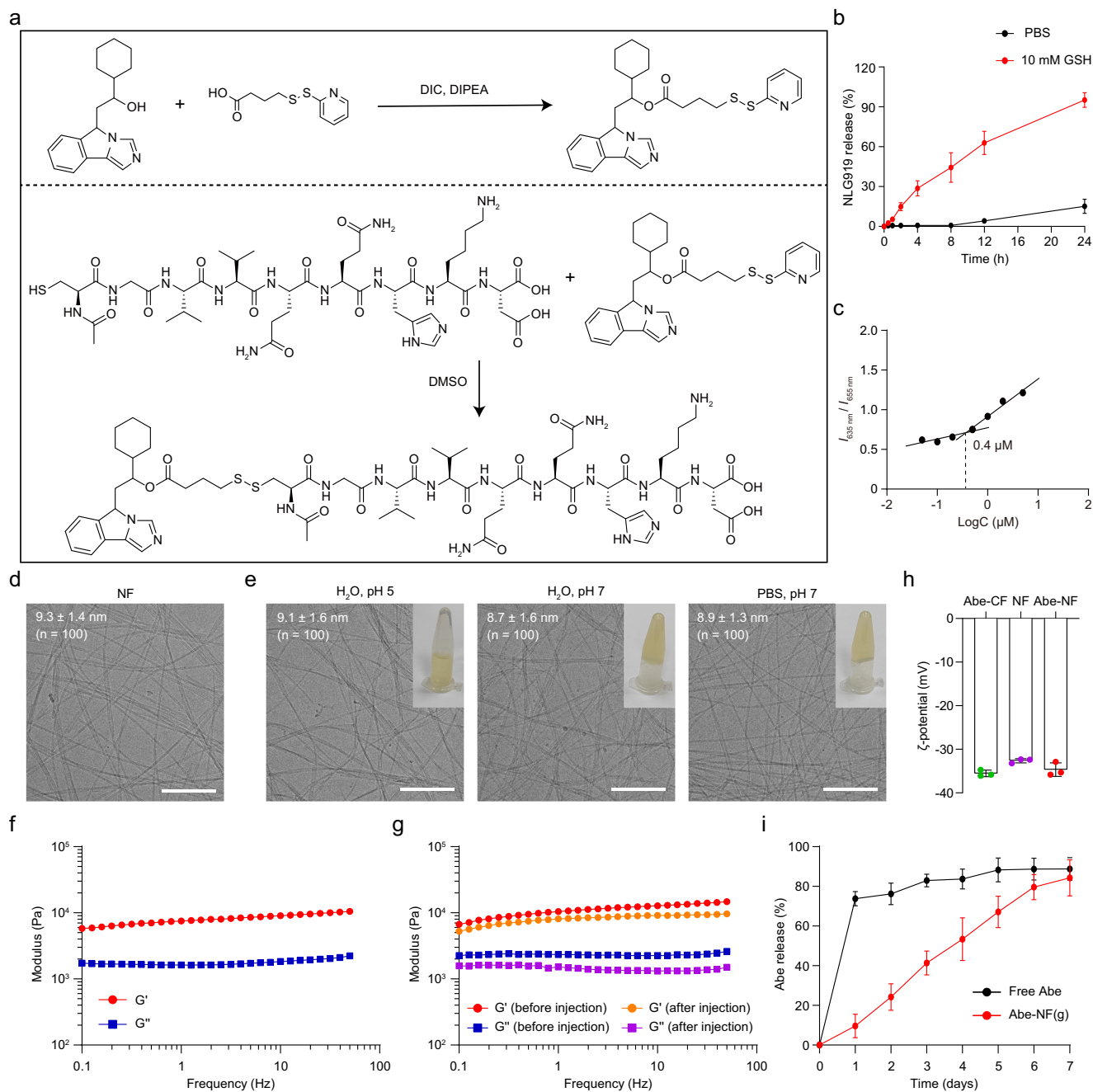


Fig. 2 | Characterization of NLG-HKD and Abe-NF(g). **a** The synthesis scheme of the peptide-drug conjugate NLG-HKD. **b** Cumulative release of NLG919 from NLG-HKD in PBS or 10 mM GSH ($n = 3$ independent experiments). **c**, **d** Critical micelle concentration (**c**) and the representative cryo-TEM image (**d**) of NLG-HKD. **e** Photographs and cryo-TEM images of the Abe-NF(g) at different pH values with or without PBS. **d**–**e** Scale bars = 200 nm. **f**–**g** Frequency sweeps of G' and G'' of Abe-NF(g) at the absence (**f**) and presence (**g**) of salts before or after injection. The

experiments were performed at 25 °C with a strain of 0.5%. **h** ζ -potentials of Abe-CF, NF, and Abe-NF ($n = 3$ independent experiments). **i** Abe release profile from the Abe-NF(g) in PBS ($n = 3$ independent experiments). The Abe solution was used as a control group. Data were presented as mean \pm SD. PBS phosphate-buffered saline, DMSO dimethyl sulfoxide, DIC diisopropylcarbodiimide, DIPEA diisopropylethylamine, GSH glutathione, Abe abemaciclib. Source data are provided as a Source Data file.

stimulating factor (M-CSF) and HMGB1 promoted progenitor cell differentiation into M1⁶¹, and indeed elevated cancer cell secretion of M-CSF and HMGB1 was observed after Abe treatment (Fig. 3g and Supplementary Fig. 11). In consistent with these results, an elevated level of interleukin-12 p70 (IL-12p70) and reduced level of interleukin-10 (IL-10) were recorded in the medium that was harvested from coculture of BMDMs and 4T1 cells pretreated with Abe-containing treatments (Fig. 3h). We further investigated the effects of Abe on CTLL-2 (a CTL cell line) and found that Abe and Abe-NF were able to increase the secretion of interleukin-2 (IL-2) by approximately 80%

(Fig. 3i) without causing obvious cytotoxicity (Supplementary Fig. 15). Similar experiments were performed using the human TNBC cell line MDA-MB-231 and the human monocyte cell line THP-1, confirming the ability of Abe-NF to induce ICD of human TNBC cells and the M1-preferred differentiation of human monocytes (Fig. 3j–m and Supplementary Fig. 10). Moreover, Abe-NF-treated MDA-MB-231 cells effectively reduced the proportion of T_{Regs} among CD4⁺ T cells enriched from human peripheral blood mononuclear cells (Fig. 3n). These results confirmed that Abe played an essential role in priming anti-tumor immunity by promoting DC maturation and macrophage

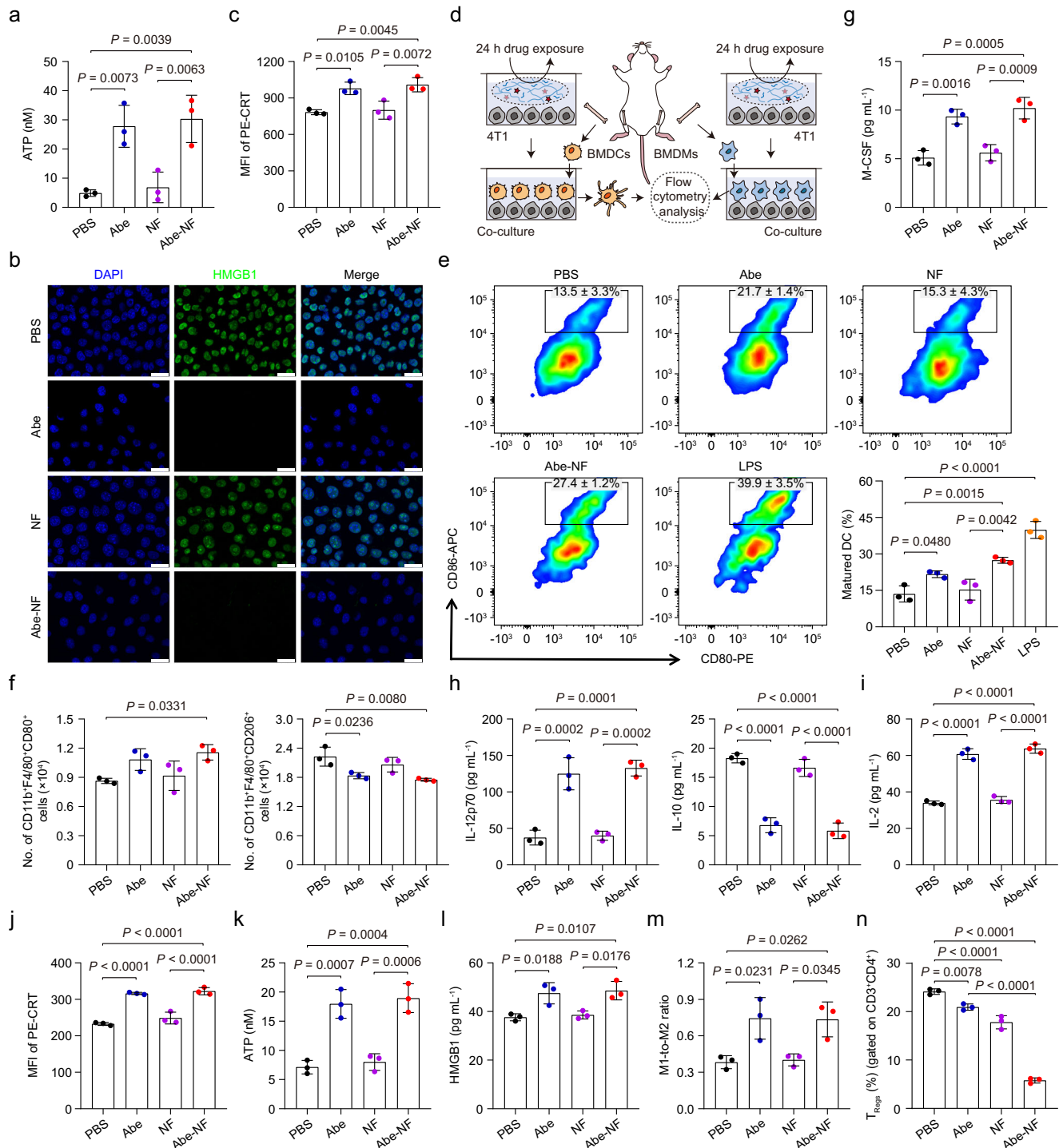


Fig. 3 | Immunological activity of Abe-NF in vitro. **a** Concentrations of ATP in the supernatant of 4T1 cells with different treatments. **b** Representative confocal images of HMGB1 in 4T1 cells. Blue, cell nucleus stained with DAPI; green, HMGB1 stained with Alexa Fluor® 488-labelled anti-HMGB1 antibody. Scale bars = 25 μm . **c** Flow cytometry analysis of CRT exposure of 4T1 cells 24 h after different treatments. MFI, mean fluorescence intensity. **d** Schematic illustration of the experimental designs. **e** Representative flow cytometric images and quantitative analysis of DC maturation in vitro 24 h after co-culture with 4T1 cells that had received different treatments. **f** Numbers of M1 and M2 in the co-culture of BMDMs and pretreated 4T1 cells. **g** Concentrations of M-CSF in the supernatant of 4T1 cells with different treatments. **h** Concentrations of IL-12p70 and IL-10 in the co-culture of BMDMs and pretreated 4T1 cells. **i** Concentrations of IL-2 in the supernatant of CTLL-2 cells after different

treatments. **j** Flow cytometry analysis of CRT exposure of MDA-MB-231 cells 24 h after different treatments. **k**, **l** Concentrations of ATP (**k**) and HMGB1 (**l**) in the supernatant of MDA-MB-231 cells with different treatments. **m** M1-to-M2 ratio of the macrophages sourced from THP-1 after a 24 h-incubation with MDA-MB-231 cells that had been pretreated with Abe, NF, or Abe-NF. **n** Proportion of T_{Regs} after being treated with supernatant of MDA-MB-231 cells that had been pretreated with different formulations for 24 h. **a–n** Data were presented as mean \pm SD ($n = 3$ independent experiments) and the statistical significance was calculated with one-way ANOVA following by the Tukey's tests. DC dendritic cell, HMGB1 high mobility group box 1, M-CSF macrophage colony-stimulating factor, CRT calreticulin, BMDCs bone marrow-derived dendritic cells, BMDMs bone marrow-derived macrophages, T_{Regs} regulatory T cells. Source data are provided as a Source Data file.

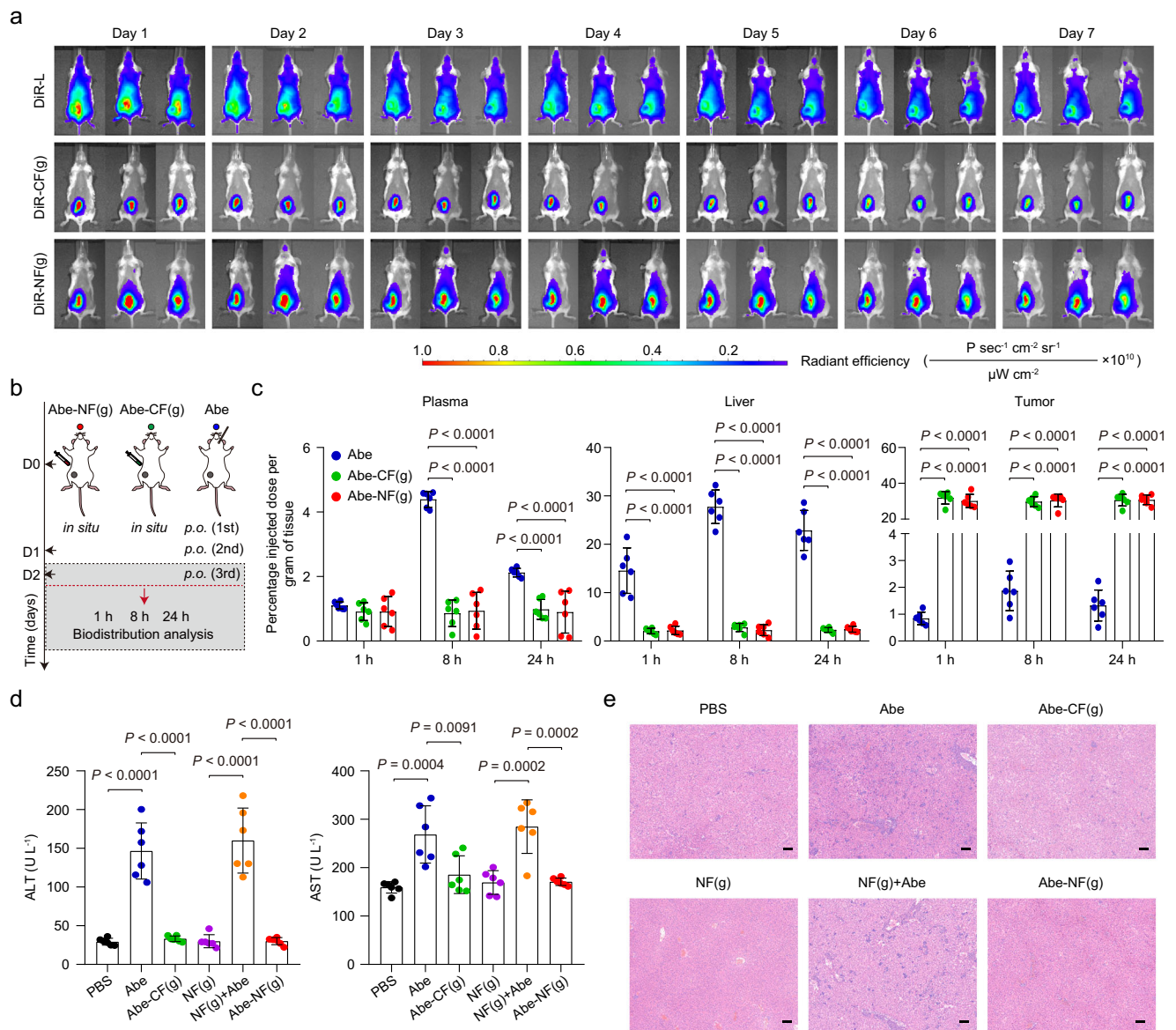


Fig. 4 | Biodistribution and biocompatibility of the drugs. **a** Retention of the DiR-labelled hydrogel or DiR-labelled liposomes at orthotopic TNBC tumors after a local injection ($n = 3$ mice). **b** Schematic illustration of the experimental design. **c** Quantification of Abe in plasma, livers, and tumors at 1 h, 8 h, and 24 h after the third oral administration of Abe ($n = 6$ mice). **d**, **e** Activities of ALT and AST in serum (**d**) and H&E stained liver sections (**e**) collected from 4T1 tumor-bearing mice 7 days

after the injection of the hydrogel ($n = 6$ mice). Scale bars = 100 μm . Data were presented as mean \pm SD and the statistical significance was calculated with one-way or two-way ANOVA following by the Tukey's tests. ALT alanine transaminase, AST aspartate transaminase, TNBC tripe-negative breast cancer, H&E hematoxylin and eosin. Source data are provided as a Source Data file.

differentiation into M1, whereas, NLG919 was inert. Abe would trigger IL-2 secretion from CTLs rather than cell death, which was beneficial for cancer immunotherapy.

We further evaluated the effect of Abe on type I interferon release, as it had been reported that the loss of CDK4/6 function would lead to the secretion of type I interferon⁶², which could further upregulate IDO-1^{63,64}. Indeed, Abe and Abe-NF significantly promoted type I interferon (IFN- α and IFN- β) secretion, which, as expected, upregulated the expression of IDO-1 and the IDO-1-mediated Kyn production in 4T1 cells (Supplementary Fig. 16a–c). To elucidate the role of IDO-1 during Abe-initiated immune responses, we constructed a subline of 4T1 cells with a trace amount of IDO-1 (4T1^{IDO-1 KO}) and found that Abe was also able to induce type I interferon secretion of 4T1^{IDO-1 KO} cells, but failed to upregulate IDO-1 expression and Kyn production (Supplementary Fig. 16d–g). These results demonstrated that Abe could not only induce 4T1 cell secretion of type I interferon, which was important

for priming anti-tumor immunity, but could also upregulate immunosuppressive molecules, such as IDO-1, which was consistent with our previous study⁶⁵.

Biodistribution and toxicity of Abe-NF(g)

We expected that Abe-NF(g) would be retained at the site of injection for a prolonged period and reduce the systemic side effects of Abe. Therefore, we first investigated the biodistribution of DiR-labelled NF(g) in vivo using a DiR-labelled C₁₆-CGVVQHKD nanofiber hydrogel (DiR-CF(g)) and DiR-labelled liposomes (DiR-L) as controls. Live animal imaging revealed that both hydrogels showed prolonged retention in tumors during the investigation period, whereas DiR-L showed a diffuse distribution and relatively fast clearance after injection (Fig. 4a). Based on the above results, we directly monitored Abe exposure on day 2 after hydrogel implantation in the plasma, tumors, and major organs of mice, using orally dosed Abe as a control (Fig. 4b). Higher

Abe exposure was recorded in most major organs and plasma from mice receiving free Abe than in those from Abe-NF(g)- or Abe-CF(g)-treated mice, especially 8 h after the last oral administration. In contrast, the intratumoral concentrations of Abe in the hydrogel-treated mice were at least 10-fold higher than those in the free Abe-treated mice (Fig. 4c and Supplementary Fig. 17a), with higher tumor-to-tissue ratios (Supplementary Table 1). Similar results were observed when analyzing the concentrations of NLG919 in tumors compared to those in the plasma from mice receiving Abe-NF(g) (Supplementary Fig. 17b). These results demonstrated that our supramolecular hydrogels were able to maintain a higher drug concentration in tumors and limit systemic exposure.

We then investigated the potential toxicity of the different formulations. Since higher liver exposure to Abe was observed in the orally administered group, elevated serum alanine transaminase and aspartate transaminase levels were recorded, whereas no significant difference was observed in blood urea nitrogen and creatinine levels (Fig. 4d and Supplementary Fig. 18), indicating potential damage in the livers but not in the kidneys. Further histological examination of the major organs confirmed this finding, and increased immune cell infiltration was observed in the livers of mice receiving orally dosed Abe (Fig. 4e and Supplementary Fig. 19). In addition, a decrease in the density of blood lymphocytes was also recorded in mice receiving orally dosed Abe, whereas Abe-CF(g) and Abe-NF(g) did not cause significant changes in blood cell counts (Supplementary Table 2). These results clearly demonstrated that Abe-CF(g) and Abe-NF(g) could significantly reduce systemic Abe exposure and reduce potential toxicity to the livers and immune cells.

Immune responses in vivo

Given the potent activity of Abe-NF(g) on BMDCs and BMDMs in vitro, we first investigated the influence of Abe-NF(g) on the DC maturation and macrophage polarization in vivo. Flow cytometry analysis revealed that DC maturation in draining lymph nodes (DLN) was significantly elevated by Abe-NF(g) (1.2-fold) and Abe-CF(g) (1.3-fold) in comparison with that in the PBS-treated group (9.4%) (Fig. 5a and Supplementary Fig. 20). Notably, Abe and NF(g)+Abe only showed mild activity, whereas NF(g) showed no obvious efficacy. Similar trends were observed while determining the concentrations of tumor necrosis factor- α (TNF- α), interferon- γ (IFN- γ), and IL-12p70 in the DLNs, which were upregulated by 1.3-fold, 1.1-fold, and 2.5-fold by Abe-NF(g), respectively (Supplementary Fig. 21). In the case of tumor-associated macrophages (TAMs), the density of TAMs was not influenced by any of the treatments (Supplementary Fig. 22). However, the density of M1 was increased by Abe-NF(g) and Abe-CF(g), which two treatments decreased the density of M2, leading to a 1.0-fold increase in the M1-to-M2 ratio by Abe-NF(g) (Fig. 5b). Consistently, the two treatments upregulated intratumoral levels of IL-12p70 and downregulated IL-10 (Fig. 5c). These results suggested that DC maturation and M1 polarization were mainly enhanced by Abe rather than by NLG919, the efficacy of which could be maximized when delivered using hydrogels that prolonged Abe exposure of the tumors.

Given that IDO-1 is an inducible enzyme that creates an immunosuppressive microenvironment by converting tryptophan into kynurenine, we explored the effects of Abe-NF(g) on IDO-1 expression and Kyn production. In comparison with PBS, all Abe-containing treatments significantly elevated the expression of intratumoral IDO-1 by at least two folds, with orally dosed Abe and hydrogel-encapsulated Abe showing comparable efficacies (Fig. 5d and Supplementary Fig. 23). In sharp contrast, only Abe-CF(g) increased the Kyn-to-Trp ratio, whereas the other treatments showed no significant effect (Fig. 5e and Supplementary Fig. 24). Importantly, the Kyn-to-Trp ratio was much lower in Abe-NF(g)-treated tumors than that in Abe-CF(g)-treated tumors. These results suggested that NLG919 could effectively

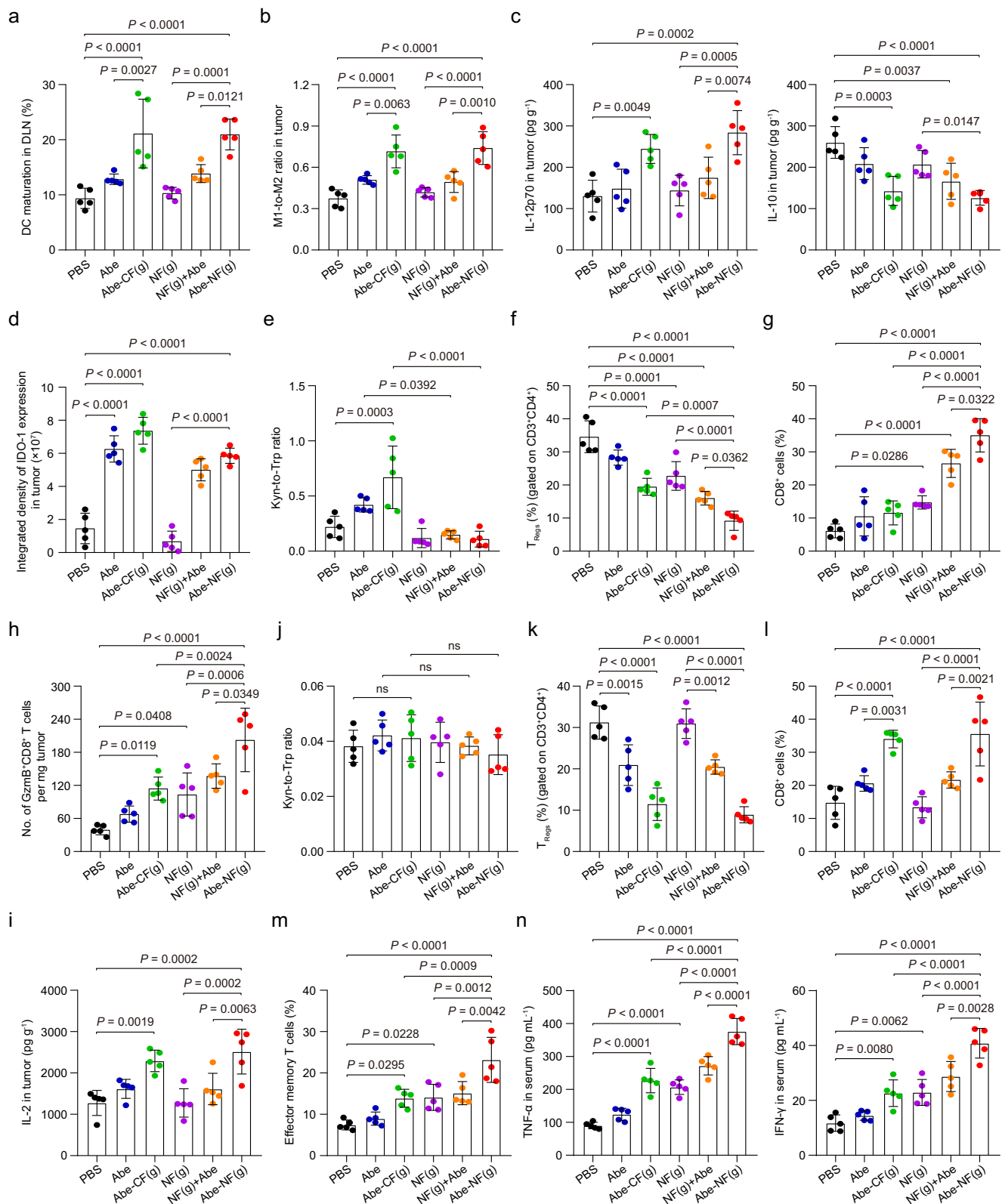
inhibit the activity of IDO-1, even though the expression of this protein would be upregulated by Abe.

We further determined the changes in intratumoral lymphocytes using flow cytometry. We found that all the treatments, except free Abe, reduced the proportion of T_{Reg} among the intratumoral CD4⁺ T lymphocytes, Abe-NF(g) being the most effective (showing a 73.5% reduction) (Fig. 5f and Supplementary Fig. 25). Abe-NF(g) also increased the percentage of CTLs (CD8⁺) among the intratumoral CD3⁺ T lymphocytes (Fig. 5g and Supplementary Fig. 26) and the density of active CTLs (CD8⁺GzmB⁺) by 4.1-fold (Fig. 5h). In addition, Abe-NF(g) effectively upregulated the expression of IL-2 (Fig. 5i). Notably, all NLG919-containing treatments significantly increased the intratumoral density of active CTLs, indicating the important role of the drug in modulating CTL activity through inhibition of IDO-1 activity. Abe-CF(g) was more effective than free Abe in increasing the infiltration of active CTLs and the concentration of IL-2, suggesting that the localized and sustained delivery of Abe was beneficial in priming CTLs. In contrast, the intratumoral Kyn-to-Trp ratios were comparable among all the treated mice bearing 4T1^{IDO-1 KO} tumors (Fig. 5j). Abe-containing groups still reduced the proportion of T_{Regs}, whereas further inclusion of NLG919 showed no additional benefits (Fig. 5k). Increased CTLs infiltration was consistently observed in Abe-treated 4T1^{IDO-1 KO} tumors, the extent of which seemed more profound than that in 4T1 tumors (Fig. 5l). These results demonstrated that treatment-induced IDO-1 hindered effective TNBC therapy, and extensive inhibition or deletion of IDO-1 could synergize with Abe.

Since Abe-NF(g) was developed as a neoadjuvant immunotherapy, we further explored the percentage of effector memory T cells (T_{EM}) among splenocytes after different treatments and inflammatory responses. Abe-NF(g) was the most effective at increasing the T_{EM} fraction, which was 2.1-fold higher than that in mice receiving PBS (Fig. 5m). As a result, the highest serum levels of TNF- α and IFN- γ were recorded in mice that were previously treated with Abe-NF(g), after being rechallenged with cancer cells (Fig. 5n). The percentage of spleen T_{EM} and the levels of serum TNF- α and IFN- γ seemed to be positively associated with the intratumoral density of active CTLs, highlighting the importance of combination therapy using localized Abe and NLG919.

Anti-tumor efficacy in vivo

Given the potent efficacy of Abe-NF(g) in priming anti-tumor immunity, we further evaluated its therapeutic efficacy. Ideally, tumors should be resected as early as possible after the activation of immune responses. According to our preliminary study, DC maturation was recorded on day 7 rather than on day 3 after hydrogel treatment (data not shown). Therefore, we performed tumor resection 7 days after hydrogel administration in our subsequent experiments. First, we evaluated the anti-tumor efficacy of Abe-NF(g) in a recurrence model (Fig. 6a). After the neoadjuvant immunotherapy and subsequent tumor resection, Abe-NF(g) was the most effective among the tested treatments, as evidenced by the slowest tumor regrowth (Fig. 6b), the lowest bio-illumination signals (Fig. 6c and Supplementary Fig. 27), the smallest sizes and weights of the recurrent tumors (Fig. 6d and Supplementary Fig. 28) in mice receiving Abe-NF(g). Based on the tumor recurrence growth curve, the inhibition rates were > 90%, 84%, 66%, 61%, and 30% for Abe-NF(g), NF(g)+Abe, NF(g), Abe-CF(g), and Abe, respectively. Moreover, terminal deoxynucleotidyl transferase-mediated dUTP nick-end-labeling (TUNEL) analysis of the tumor sections confirmed that Abe-NF(g) induced the most extensive cell apoptosis compared with the other treatments (Fig. 6e and Supplementary Fig. 29). None of the treatments affected the body weight of the mice obviously (Supplementary Fig. 30), indicating that they did not cause severe side effects. To further confirm the essential role of anti-tumor immunity in Abe-NF(g)-mediated TNBC therapy, the



therapeutic effect of the hydrogel was assessed in a recurrence model using NOD-SCID mice. In sharp contrast to the above results, only Abe-CF(g) and Abe-NF(g) showed significant but mild efficacy in tumor growth inhibition and animal survival elongation (Supplementary Fig. 3I), which might be associated with the inhibition of cancer cell proliferation by Abe. These results demonstrated that Abe-NF(g) exerted anti-tumor effects mainly by activating anti-tumor immunity.

Pulmonary metastasis is one of the major causes of death in TNBC. Therefore, we further evaluated the anti-tumor efficacy of Abe-NF(g) in a pulmonary metastasis model (Fig. 6f). Mice that received neoadjuvant therapy with Abe-NF(g) and surgical resection showed the lowest rate of pulmonary metastasis within 6 weeks (one out of eight), followed by NF(g)+Abe (four out of eight), NF(g) (five out of eight), Abe-CF(g) (six out of eight), and Abe (eight out of eight) (Fig. 6g, h). Indeed,

Fig. 5 | Anti-tumor immunity in vivo. **a** Proportion of matured DCs in DLN was analyzed using flow cytometry 7 days after the injection of the hydrogels. **b, c** Examination of M1-to-M2 ratio (**b**) and quantification of the intratumoral cytokines (**c**) after different treatments. **d, e** IDO-1 expression (**d**) as well as the Kyn-to-Trp ratio (**e**) in tumors were measured 7 days after the injection of the hydrogel. **f–h** Intratumoral percentage of the T_{Reg} (**f**) and CD8⁺ T lymphocytes (**g**) in addition to the densities of CD8⁺GzmB⁺ T cells (**h**) after being treated with different formulations. **i** Levels of IL-2 in tumors after different treatments. **j** The Kyn-to-Trp ratio in 4T1^{IDO-1 KO} tumors was measured 7 days after the injection of the hydrogel.

k, l The percentage of T_{Reg} (**k**) and CD8⁺ T lymphocytes (**l**) in 4T1^{IDO-1 KO} tumors after being treated with different formulations. **m** Flow cytometry analysis of splenic T_{EM} 7 days after the removal of primary tumors. **n** Concentrations of TNF- α and IFN- γ in serum 3 days after the re-challenge of 4T1 cells. **a–n** Data were presented as the mean \pm SD ($n = 5$ mice) and the statistical significance was calculated with one-way ANOVA following by the Tukey's tests. DC dendritic cell, DLN draining lymph node, Kyn kynurenine, Trp tryptophan, IDO-1 indoleamine 2,3-dioxygenase 1, T_{Reg} regulatory T cell, TNF- α tumor necrosis factor- α , IFN- γ interferon- γ , IL-12p70 interleukin-12 p70. Source data are provided as a Source Data file.

Abe-NF(g) prolonged the median survival time of mice from 35 days (PBS group) to 74 days, and was the most effective among the tested treatments (Fig. 6i). Additional experiments were performed to examine metastasis to the lungs, which were harvested from the mice 4 weeks after hydrogel implantation. Histological analysis of the lungs, in addition to the analysis of the number of metastatic sites, exhibited that Abe-NF(g) reduced lung metastasis by 92% (Fig. 6j), evidenced by the reduced bio-illumination signals in the lungs of Abe-NF(g)-treated mice (Supplementary Fig. 32) and the absence of noticeable micro-metastatic sites in the histological sections of the lungs (Fig. 6k). These results demonstrated that neoadjuvant immunotherapy using Abe-NF(g) protected mice from distant tumor metastasis, possibly via an established anti-tumor immune memory. The combined and localized use of Abe and NLG919 was more beneficial than the two monotherapies.

Discussion

Immunotherapy has revolutionized the field of cancer therapy and is effective as a monotherapy for the treatment of certain types of cancers, such as melanoma and lung cancer. However, in the case of TNBC, immune checkpoint blockade is ineffective as a monotherapy¹ and should be used in conjunction with Abraxane as a neoadjuvant therapy⁶⁶. Nevertheless, the improvement in patient survival after combinatorial therapy is moderate, and a better prognosis is usually observed in patients with higher CTL infiltration⁶⁷, highlighting the importance of priming anti-tumor immunity. Unfortunately, current systemic chemotherapy commonly induces myelosuppression and activates immunosuppressive pathways. Here we demonstrate a drug depot strategy to simultaneously prime anti-tumor immunity and inhibit treatment-induced IDO-1 by creating an injectable supramolecular hydrogel of Abe-loaded peptide-NLG919 nanofibers, termed Abe-NF(g). A suitable concentration of hydrogel (15 mM in NLG-HKD) is critical for its application, as linear and sustainable drug release over a period of 7 days can only be achieved at 15 mM or above, whereas a high viscosity of 30 mM hydrogel prevents its passage through a fine needle. At 15 mM in NLG-HKD, the nanofibers entangled with each other to form a hydrogel almost instantly at neutral pH. In addition, the hydrogel recovered within 2 minutes after passing through a 27 G needle, probably because the hydrogel only fractured into domains that could easily rejoin to form a solid hydrogel⁶⁸. We showed that Abe could be locally and sustainably released from the hydrogel after injection, maintaining high drug exposure in the tumors rather than in the major organs and blood. We revealed that intratumoral Abe significantly improved DC maturation and M1-preferential macrophage polarization. We demonstrated that the liver toxicity and immune toxicity of Abe could be potentially reduced by engineering an Abe depot.

A key hurdle in neoadjuvant therapy is the activation of the immunosuppressive pathways⁶⁹. In our study, the intratumoral expression of IDO-1 was markedly upregulated, especially after prolonged exposure to Abe. IDO-1 converts Trp into Kyn, an immunosuppressive metabolite that activates T_{Reg}. PEGylated enzymes that can constantly degrade Kyn have been proven effective⁴⁴, but inhibitors of IDO-1 have failed to improve therapeutic outcomes in clinical trials⁷⁰, which may be associated with transient and low drug exposure

in tumors. Our NLG-HKD design allows prodrug molecules to self-assemble into nanofibers, which further entangle with each other to form a macroscale hydrogel. We showed that NLG919 was mainly retained in the tumors and barely entered the circulation, leading to significant inhibition of IDO-1 activity, as evidenced by the reduced intratumoral level of Kyn. Given these advantages, Abe-NF(g) successfully improved the intratumoral density of active CTLs and established anti-tumor immune memory, which retarded tumor regrowth and metastasis after surgery and prolonged survival.

Regarding the future clinical translation of this platform, the supramolecular prodrug hydrogel strategy has unique advantages as the nanofibers are formed by chemically well-defined molecules and Abe can be entrapped through a co-assembly method. With advances in imaging-guided therapy, the application of local neoadjuvant immunotherapy will be possible in TNBC and other types of cancer. We envision that the described strategy of locally priming anti-tumor immunity and relieving the immunosuppressive microenvironment can be generalized to treat tumors that are unsuitable for surgical resection at the time of diagnosis.

Methods

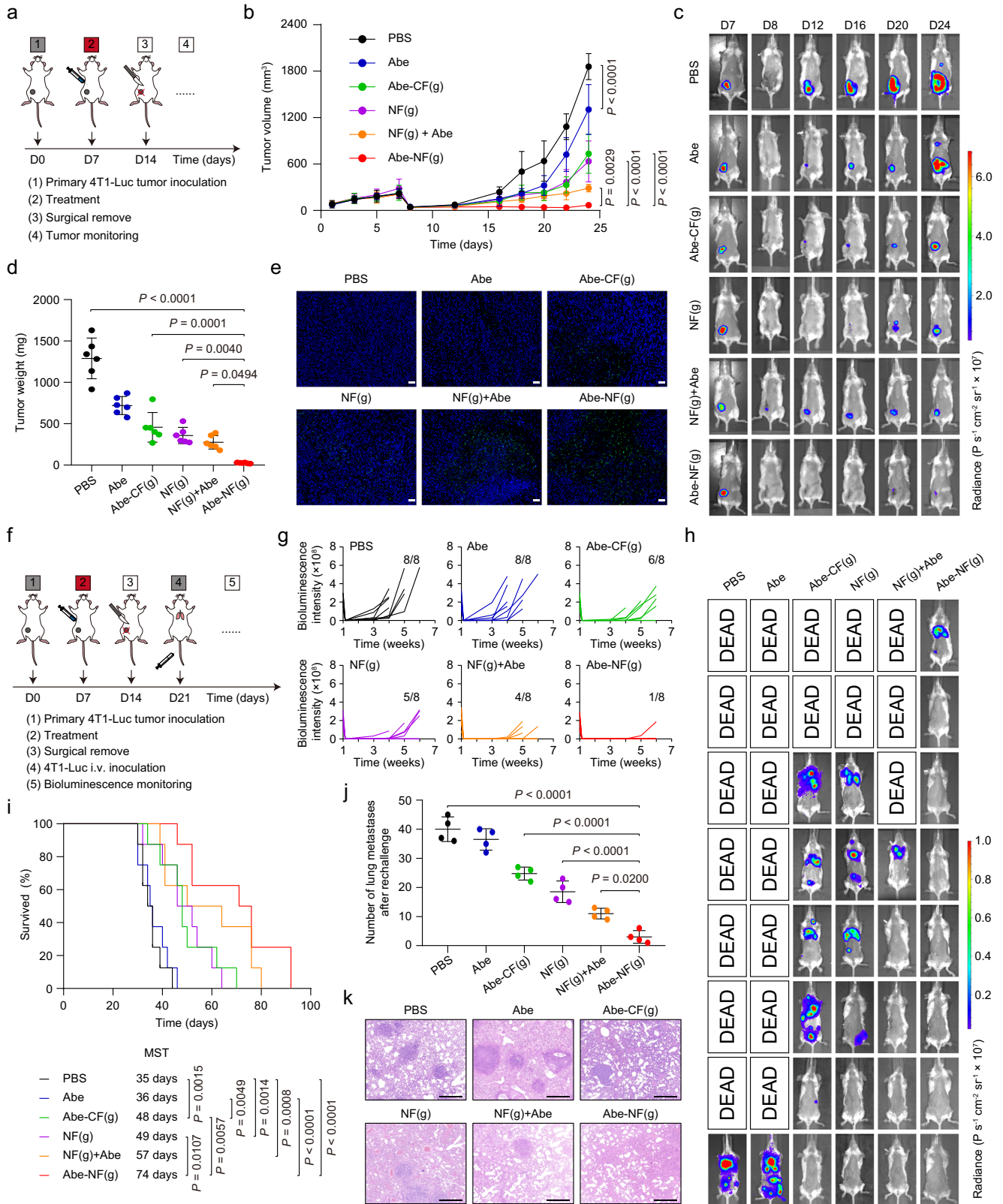
This research complies with all relevant ethical regulations approved by the Institutional Animal Care and Use Committee (IACUC) of the Shanghai Institute of Materia Medica, Chinese Academy of Sciences.

Materials

NLG919, abemaciclib (Abe) and 4-(Pyridin-2-ylidysulfanyl) butanoic acid (HO₂C-BuSS-Pyr) were purchased from Jiangsu Aikon Biopharmaceutical R&D Co., Ltd (Nanjing, China). Abemaciclib mesylate was purchased from Shanghai Coupling Pharmaceutical Technology Co., Ltd (Shanghai, China). Ac-CGVVQHKD and C₁₆-CGVVQHKD peptides (purity > 95%) were synthesized by Anhui Guoping Pharmaceutical Co., Ltd. (Hefei, China). L-Glutathione reduced was purchased from Shandong Sparkjade Biotechnology Co., Ltd. (Shandong, China). DiR dye, DiD dye, tryptophan, and kynurenine were purchased from Meilun Biotechnology (Dalian, China). D-Luciferin, Potassium Salt (40902ES03) was obtained from Yeasen (Shanghai, China). M-CSF, IL-4, and GM-CSF were purchased from Dakewe Biotech Co., Ltd. (Shenzhen, China). ELISA kits for M-CSF, IL-12p70, IL-10, IL-2, TNF- α , and IFN- γ were obtained from Neobioscience Technology Co., Ltd. (Shenzhen, China). ELISA kits for HMGB1 were purchased from Beijing Solarbio Science & Technology Co., Ltd. (Beijing, China). ATP assay kit was purchased from Beyotime Biotechnology Co., Ltd. (Shanghai, China). Hydrogenated soy phosphatidylcholine (HSPC), cholesterol, and DSPE-MPEG₂₀₀₀ were obtained from AVT Shanghai Pharmaceutical Tech Co., Ltd. (Shanghai, China). Other reagents were all obtained from Sinopharm Chemical Reagent Co., Ltd. (Shanghai, China) unless otherwise indicated.

Cells and animals

The murine TNBC cell line 4T1 cells (cat. no. SCSP-5056) were purchased from the Cell Bank of Shanghai, Chinese Academy of Sciences (Shanghai, China). The murine cytotoxic T cell line CTLL-2 cells were originally obtained from the American Type Culture Collection (America). The human TNBC cell line MDA-MB-231 cells (cat. no.



FH0213) were purchased from Shanghai Fuheng Biotechnology Co., Ltd (Shanghai, China). The human monocytic leukemia cell line THP-1 cells (cat. no. iCell-h213) were purchased from iCell Bioscience Inc (Shanghai, China). The human CD4⁺ T cells (cat. no. SCI325) sourced from human peripheral blood mononuclear cells were purchased from Yuchi Biotechnology Co., Ltd (Shanghai, China). The 4T1^{CDK4/6 KO} and 4T1^{IDO-1 KO} cells were established from 4T1 cells using CRISPR-Cas9

genome editing by Prof. Helen He Zhu's lab in Ren Ji Hospital and the lentiviruses were purchased from Hanbio Tech (Shanghai, China). The luciferase-expressing cell line 4T1-luc cells (cat. no. Hyc3607) were obtained from OBiO Technology Co., Ltd. (Shanghai, China). All the cell lines were authenticated by the suppliers using STR analysis and no mycoplasma contamination was found. The 4T1 cells, 4T1-luc cells, 4T1^{CDK4/6 KO} cells, and 4T1^{IDO-1 KO} cells were cultured in RPMI 1640

Fig. 6 | Recurrence and pulmonary metastasis of 4T1-luc tumors. **a** Schematic illustration of the tumor recurrence study. **b–e** Tumor growth profiles (**b**), representative bio-luminescent images (**c**), tumor weights (**d**), and images of TUNEL-stained tumor sections (**e**) of mice bearing 4T1-luc tumors after different treatments ($n = 6$ mice). Scale bars = 50 μm . **f** Schematic illustration of the design of the pulmonary metastasis inhibition experiment. **g–i** Changes in the intensities of bio-illumination signals (**g**), bio-illumination images of mice at day 42 (**h**), and survival curve (**i**) of mice bearing 4T1-luc tumors after different treatments ($n = 8$ mice). **j, k** Numbers of lung metastasis (**j**) and representative images of H&E-stained lung

sections (**k**) from mice bearing 4T1-luc tumors at day 28 after different treatments ($n = 4$ mice). Scale bars = 500 μm . Data were presented as the mean \pm SD and the statistical significance was calculated with one-way ANOVA following by the Tukey's tests for tumor weights and numbers of lung metastasis. Two-way ANOVA following by the Tukey's tests was used to analyze the tumor growth in the recurrence model and the survival curve was statistically analyzed with the log-rank tests. MST median survival time, H&E hematoxylin and eosin, TUNEL terminal deoxynucleotidyl transferase-mediated dUTP nick-end-labeling. Source data are provided as a Source Data file.

(BasalMedia) containing 10% fetal bovine serum (FBS, Gibco), 2.5 g L^{-1} glucose (Sigma), 0.11 g L^{-1} sodium pyruvate (Beijing Solarbio Science & Technology Co., Ltd., Beijing, China) and 1% antibiotics (New Cell & Molecular Biotech Co., Ltd., Suzhou, China). The CTLL-2 cells were cultured in complete RPMI 1640 with IL-2 (100 U mL^{-1}). The MDA-MB-231 cells were cultured in L-15 (Fuheng) containing 10% FBS and 1% antibiotics at 37 °C without CO_2 . The THP-1 cells were cultured in complete RPMI 1640 with β -mercaptoethanol (50 μM). The human CD4^+ T cells were cultured in complete RPMI 1640 with β -mercaptoethanol (50 μM) and IL-2 (80 ng mL^{-1}). All the cells were maintained at 37 °C in a humidified incubator with 5% CO_2 except the MDA-MB-231 cells.

Female BALB/c mice (6–8 weeks) and female NOD-SCID mice (6–8 weeks) were purchased from Beijing HFK Bioscience. Mice were maintained on a standard diet with water ad libitum at 23 °C and 30–70% relative humidity in a 12 hours:12 hours light-dark cycle. All animal procedures were performed in accordance with the guidelines approved by the Institutional Animal Care and Use Committee of the Shanghai Institute of Materia Medica, Chinese Academy of Sciences (2021-06-LYP-43, 2022-06-LYP-44, 2023-07-LYP-45). The sex was not considered in the study design in this work. Female mice were used for all the animal assays in this study as reported in the literature studies since it focused on triple-negative breast cancer.

Synthesis of NLG-HKD

$\text{HO}_2\text{C-BuSS-Pyr}$ (500 mg) and NLG919 (308 mg) were mixed in 10 mL dichloromethane (DCM) and stirred for 24 h at room temperature in the presence of 152 mg diisopropylcarbodiimide (DIC) and 282 mg diisopropylethylamine (DIPEA). The reaction solution was diluted with 30 mL DCM and extracted with saturated sodium chloride solution. The organic phase was collected and dried with anhydrous sodium sulfate and then purified by silica gel column chromatography to obtain the NLG-Pyr, which was characterized with AVANCE III 600 (Bruker, Switzerland) and electron spray ionization mass spectrometry (ESI-MS, Finnigan LTQ linear ion-trap mass spectrometer, Finnigan, USA). The purity of NLG-Pyr was also determined with ultra-performance liquid chromatography (UPLC, Waters, USA), which was eluted by acetonitrile and water containing 0.1% trifluoroacetic acid (wavelength: 254 nm; flow rate: 0.3 mL min^{-1}). Ac-CGVVQHKD peptide (100 mg) and NLG-Pyr (51 mg) were dissolved in 10 mL anhydrous dimethyl sulfoxide (DMSO) and stirred at room temperature under an inert atmosphere for 3 days. The reaction solution was then diluted with an equal volume of methanol and extracted with diethyl ether. After removing the ether, the crude product was purified with preparative HPLC, which was eluted by acetonitrile and water containing 0.1% trifluoroacetic acid (wavelength: 220 nm; flow rate: 10 mL min^{-1}), and fractions containing only the target molecules were combined, concentrated and freeze-dried for 2 days. The purified NLG-HKD was identified with ESI-MS and the purity of it was determined with UPLC as well.

Preparation and characterization of Abe-NF(g)

NLG-HKD (15 mM) and Abe (1.5 mM) were first dissolved in 2 mL hexafluoroisopropanol (HFIP). After removing the solvent, the remaining

materials were reconstituted with deionized water and the pH was adjusted to 7 using NaOH solution (0.5 mM), and then mixed with 10 \times PBS (9 : 1, vol/vol) to obtain Abe-NF(g). Abe-CF(g) and NF(g) were prepared using a similar procedure. Abemaciclib mesylate was used in the free Abe group in the following experiments. For an easy dosage comparison, the concentrations of abemaciclib instead of Abemaciclib mesylate were used in the following experiments. The morphologies of Abe-NF(g), Abe-CF(g), and NF(g) were examined on an electron microscope (FEI, Talos Arctica G2, USA) at an accelerating voltage of 200 kV after the hydrogels were diluted to 1 mM with water. The rheological property of the Abe-NF(g) was determined on a rheometer (TA, ARES-G2, USA) 24 h after the sample preparation. All measurements were conducted in a steady-state shear sweep mode at a temperature of 25 °C. G' and G'' were all determined with a frequency range of 0.1–50 Hz. The release behaviors of NLG-HKD and Abe from the hydrogels of different concentrations were detected at 37 °C in PBS for 7 days. The concentration of Abe in the free Abe group (1.5 mM) was comparable to that in the 15 mM hydrogel and all the samples were determined with UPLC.

Cell viability

4T1 cells, CTLL-2 cells, MDA-MB-231 cells and 4T1^{CDK4/6 KO} cells were seeded in 96-well plates (3×10^3 cells/well) overnight. The medium was then replaced with a fresh medium containing Abe or Abe-NF of different concentrations. After a 24 h-incubation, the viability of the cells was measured by Cell counting kit-8 (C6005, New Cell & Molecular Biotech Co., Ltd., Suzhou, China) according to the manufacturer's protocol. In another experiment, the CTLL-2 cells were seeded in a 24-well plate (2×10^5 cells/well) and were incubated with Abe, NF (NLG919: 100 μM) and Abe-NF (Abe: 10 μM) respectively for 24 h. The concentrations of IL-2 in the supernatants were determined using an ELISA kit.

Immunogenic cell death

4T1 cells, MDA-MB-231 cells, and 4T1^{CDK4/6 KO} cells were seeded into a 24-well plate (1×10^5 cells/well) and allowed to attach overnight. The cells were then treated with Abe, NF (NLG919: 100 μM), or Abe-NF (Abe: 10 μM) for 24 h at 37 °C before further analysis. To quantify the surface exposure of CRT on different cells, the cells were harvested, then stained with anti-CRT-PE antibody (CST, cat. no. #19780, 1:500 dilution) for 30 min, and analyzed using a Fortessa flow cytometer. To observe the subcellular location of CRT, 4T1 cells were fixed and sequentially stained with Wheat Germ Agglutinin Alexa Fluor 647 conjugate (Invitrogen, cat. no. W32466), anti-CRT antibody (Abcam, cat. no. ab2907, 1:250 dilution), Alexa Fluor® 488 Goat Anti-Rabbit IgG H&L (Abcam, cat. no. ab150077, 1:500 dilution), and DAPI. To observe the subcellular localization of HMGB1, the cells were fixed and permeabilized and then sequentially stained with the primary antibody against HMGB1 (Abcam, cat. no. ab79823, 1:250 dilution), Alexa Fluor® 488 Goat Anti-Rabbit IgG H&L (Abcam, cat. no. ab150077, 1:500 dilution), and DAPI. The cells were imaged on a confocal microscopy Leica TCS SP8 (Leica, Germany). The extracellular ATP, HMGB1, and M-CSF in the supernatant were determined by ATP assay kit (S0026, Beyotime, Shanghai, China) and corresponding ELISA kits, respectively.

DC maturation in vitro

Bone marrow cells were collected from female BALB/c mice and then seeded in a 24-well plate with RPMI 1640 medium containing IL-4 (20 ng mL⁻¹) and GM-CSF (10 ng mL⁻¹) for 6 days to obtain BMDCs. 4T1 cells (1 × 10⁵ cells/well in a 24-well plate) or 4T1^{CDK4/6 KO} cells were pretreated with Abe, NF (NLG919: 100 μM) or Abe-NF (Abe: 10 μM) for 24 h, and then incubated with BMDCs for another 24 h. The cells were then stained with Zombie UV Fixable Viability Kit (Biolegend, cat. no. 423108, 1:200 dilution), anti-CD11c-FITC (TONBObiosciences, cat. no. 35-0114-U025, 1:100 dilution), anti-CD80-PE (TONBObiosciences, cat. no. 50-0801-U025, 1:100 dilution) and anti-CD86-APC (TONBObiosciences, cat. no. 20-0862-U025, 1:100 dilution) antibodies, before analyzing using a Fortessa flow cytometer. LPS (4 μg mL⁻¹)-treated BMDCs were used as a positive control in this experiment.

Differentiation of BMDMs and THP-1 sourced macrophages in vitro

The bone marrow cells were collected from the female BALB/c mice and then cultured in a 12-well plate using DMEM medium containing M-CSF (20 ng mL⁻¹) for 6 days. 4T1 cells were pretreated with Abe, NF (NLG919: 100 μM) or Abe-NF (Abe: 10 μM) for 24 h, and incubated with BMDMs for another 24 h. Concentrations of IL-12p70 and IL-10 in the supernatant were quantified using the ELISA kits as well according to the manufacturer's protocols. The cells were then stained with antibodies against Zombie UV dye, against CD11b (TONBObiosciences, cat. no. 65-0112-U100, 1:100 dilution), against F4/80 (Biolegend, cat. no. 123108, 1:100 dilution), against CD80 (TONBObiosciences, cat. no. 50-0801-U025, 1:100 dilution), and against CD206 (eBiosciences, cat. no. 17-2061-82, 1:100 dilution) before analyzing using a Fortessa flow cytometer (USA). The THP-1 cells were induced with phorbol 12-myristate 13-acetate (MedChemexpress) to obtain macrophages. MDA-MB-231 cells were pretreated with Abe, NF (NLG919: 100 μM) or Abe-NF (Abe: 10 μM) for 24 h, and incubated with macrophages obtained above for another 24 h. The cells were then stained with antibodies against Zombie UV dye, against CD11b, against CD80 (TONBObiosciences, cat. no. 50-0809-T100, 1:40 dilution), and against CD206 (eBiosciences, cat. no. 17-2069-42, 1:40 dilution) before analyzing using a Fortessa flow cytometer (USA).

Retention of the hydrogel

To study the retention of the hydrogel in vivo, 4T1-luc cells (1 × 10⁶ in 100 μL) were inoculated at the fourth right mammary gland of female BALB/c mice. After the tumors reached around 100 mm³ in size, the mice were randomly divided into three groups, receiving DiR-L, DiR-CF(g), or DiR-NF(g) (DiR dye: 0.5 mg kg⁻¹). The presence of the formulations was monitored every day for 7 days using an IVIS Spectrum Imaging System (Perkin Elmer, λ_{ex}/λ_{em} = 745/800 nm). The DiR-L was prepared using a lipid film (HSPC: cholesterol: DSPE-MPEG₂₀₀₀ = 5: 2: 2, m/m) hydration and membrane extrusion method. The DiR-labelled hydrogels were prepared using a similar procedure as described above except that DiR was used instead of Abe.

Biodistribution

4T1 cells (1 × 10⁶ in 100 μL) were inoculated at the fourth right mammary gland of female BALB/c mice. After the tumors reached around 100 mm³ in size, the mice were randomly divided into three groups, receiving Abe (90 mg kg⁻¹ Abe, once a day for 3 days, *p.o.*), Abe-CF(g) or Abe-NF(g) (5.7 mg kg⁻¹ Abe, one dosage, in situ). The blood, tumors, and major organs including hearts, livers, spleens, lungs, and kidneys were collected 1 h, 8 h, and 24 h after the last dose of free Abe. The tumors and other organs were weighed, cut, and homogenized in methanol to extract Abe. Abe in the plasma was also extracted using methanol. All the samples were then quantified with UPLC (Waters, USA).

In vivo cytokine analysis and measurement of Kyn and Trp

Tumor-bearing mice were established as described before. After the sizes of tumors reached around 100 mm³, the mice were randomly divided into six groups, receiving PBS, Abe (90 mg kg⁻¹ Abe, once a day for 7 days, *p.o.*), Abe-CF(g) (5.7 mg kg⁻¹ Abe, in situ), NF(g) (31.8 mg kg⁻¹ NLG919, in situ), NF(g)+Abe (31.8 mg kg⁻¹ NLG919, in situ; 90 mg kg⁻¹ Abe, once a day for 7 days, *p.o.*) and Abe-NF(g) (5.7 mg kg⁻¹ Abe, 31.8 mg kg⁻¹ NLG919, in situ). Seven days after the treatments, the mice were euthanized and the tumors were collected, weighed, homogenized, and centrifuged to quantify the concentrations of IL-2, IL-10, and IL-12p70 by ELISA kits according to the manufacturer's protocols. In a separate study, the tumors were homogenized in PBS containing 10% trichloroacetic acid to determine the concentrations of Kyn and Trp with UPLC.

Concentrations of cytokines in the serum were measured in a tumor rechallenge experiment. Briefly, mice were treated with the same strategy described above. Seven days after the treatments, the 4T1 tumors were removed. After another 7 days, 5 × 10⁵ 4T1 cells were injected via tail veins, 3 days after which the blood was collected. The concentrations of TNF-α and IFN-γ in the serum were determined using ELISA kits according to the manufacturer's instructions.

Immunoassay

The tumor-bearing mice were randomly divided into six groups and were treated with different formulations as described above. The DLNs and the tumors were collected 7 days after the treatments. The DLNs were ground to obtain the single-cell suspension, which was stained with Zombie UV Dye, anti-CD45-APC-Cy7 (eBioscience, cat. no. 47-0451-82, 1:100 dilution), anti-CD11c-FITC, anti-CD80-PE, and anti-CD86-APC antibodies and then analyzed on a flow cytometer for DC maturation analysis. The tumors were weighed and digested in RPMI 1640 medium containing collagenase IV, hyaluronidase, and DNase I to obtain the single-cell suspensions. After filtering through 70 μm cell strainers, the cells were counted and incubated with different antibodies for the flow cytometry analysis. For the tumor-associated macrophages, cells were first blocked with CD16/CD32 (TONBObiosciences, cat. no. 70-0161-U100, 1:100 dilution) and then stained with Zombie UV dye, anti-CD45-APC-Cy7, anti-CD11b-PerCP-Cy5.5 (TONBObiosciences, cat. no. 65-0112-U100, 1:100 dilution), anti-F4/80-FITC (Biolegend, cat. no. 123108, 1:100 dilution), anti-CD80-PE (TONBObiosciences, cat. no. 50-0801-U025, 1:100 dilution) and anti-CD206-APC (eBioscience, cat. no. 17-2061-82, 1:100 dilution). The ratio of M1-like macrophages (CD11b⁺F4/80⁺CD80⁻) to M2-like macrophages (CD11b⁺F4/80⁺CD206⁺) was calculated. For the analysis of active CTLs, cells were stained with Zombie UV dye, anti-CD45-APC-Cy7, anti-CD3-FITC (Biolegend, cat. no. 100204, 1:100 dilution), anti-CD8-PerCP-Cy5.5 (TONBObiosciences, cat. no. 65-0081-U100, 1:100 dilution) and anti-granzyme B-PE (eBioscience, cat. no. 12-8898-80, 1:100 dilution). For the analysis of T_{Reg} cells were stained with Zombie UV dye, anti-CD45-APC-Cy7, anti-CD3-FITC, anti-CD4-PE-Cy7 (eBioscience, cat. no. 25-0041-82, 1:100 dilution), and anti-Foxp3-PE (TONBObiosciences, cat. no. 50-5773-U025, 1:100 dilution). To analyze T_{EM}, the primary tumors were resected 7 days after different treatments. Seven days after the surgery, the mice were euthanized to collect the spleens, which were ground to obtain the splenocyte suspension. The cells were treated with red blood cell lysis buffer for 5 min, washed, counted, and stained with anti-CD45-APC-Cy7, anti-CD3-FITC, anti-CD8-APC (Biolegend, cat. no. 100711, 1:100 dilution), anti-CD44-PE (eBioscience, cat. no. 12-0441-81, 1:100 dilution) and anti-CD62L-PerCP-Cy5.5 (eBioscience, cat. no. 45-0621-80, 1:100 dilution) before flow cytometry analysis. The uses of antibodies were all in accordance with the manufacturer's instructions and the analyses were conducted on a Fortessa flow cytometer (USA). The data was analyzed by FlowJo software (TreeStar, 10.0.7) and the gating strategies were shown (Supplementary Fig. 33). Since the immune cell infiltration in TNBC

tumors was low, the cloud charts were used to show the trend of changes in our results for the clarity.

Anti-tumor efficacy

Tumor-bearing mice were established as described above. After the sizes of tumors reached around 100 mm³, the mice were randomly assigned to six groups receiving different treatments as described above. In a recurrence experiment, 95% of the tumors were surgically removed 7 days after the treatments. The tumor sizes were monitored and the volume (V) was calculated with the formula ($V = (L \times W \times W) / 2$), in which L was the length of tumors and W was the width of tumors. Bioluminescence images of 4T1-luc tumor-bearing mice at indicated time points were taken using an IVIS Spectrum Imaging System. The mice were euthanized when the tumor size reached 2000 mm³. At the end point of the tumor recurrence experiment, the tumors were harvested, weighed, and then sectioned for TUNEL analysis. In a pulmonary metastasis model, primary tumors were completely removed, and 5×10^5 4T1-luc cells were intravenously injected via tail veins 7 days after the surgery. Possible pulmonary metastasis was monitored using an IVIS Spectrum Imaging System. Lungs were collected, imaged, and sectioned for histological analysis at the end of the study. For the long-term survival study of lung metastasis models, mice were treated as described above and monitored for the survival curve. The maximal tumor size permitted by the ethics committee is 2000 mm³ and the maximal tumor size was not exceeded during the experiments. All the relevant experiments were ended when the tumor size reached this limit.

Statistics & reproducibility

Data were all presented as mean \pm standard deviation (SD). A two-sided Student's t -test (two-tailed) was used when two groups were compared. For the multiple comparisons (more than two groups were compared), one-way or two-way analysis of variance (ANOVA) and Tukey post-hoc tests were used. The survival benefit was determined using a log-rank test. All statistical analyses in this work were conducted using the Prism software package (GraphPad Prism 8.0). Significant differences were considered to exist if $P < 0.05$. In this study, the sample size was determined based on prior experimental experience, and the biological replicates were indicated within figure legends. Mice were randomly assigned to each experimental group. No statistical method was used to predetermine sample size. No data were excluded from the analyses. The Investigators were not blinded to allocation during experiments and outcome assessment.

Reporting summary

Further information on research design is available in the Nature Portfolio Reporting Summary linked to this article.

Data availability

The data that support the findings of this study are available within the paper, Supplementary Information, and Source Data File. Source data are provided with this paper. NMR data of NLG-Pyr is included in Supplementary Fig. 1. The mass spectra data of NLG-Pyr, CGVVQQHKD peptide, and NLG-HKD are included in Supplementary Fig. 1-3 respectively. Source data are provided with this paper.

References

- Bianchini, G., De Angelis, C., Licata, L. & Gianni, L. Treatment landscape of triple-negative breast cancer — expanded options, evolving needs. *Nat. Rev. Clin. Oncol.* **19**, 91–113 (2022).
- Nanda, R. et al. Pembrolizumab in patients with advanced triple-negative breast cancer: phase Ib KEYNOTE-012 study. *J. Clin. Oncol.* **34**, 2460–2467 (2016).
- Adams, S. et al. Pembrolizumab monotherapy for previously treated metastatic triple-negative breast cancer: cohort A of the phase II KEYNOTE-086 study. *Ann. Oncol.* **30**, 397–404 (2019).
- Dirix, L. Y. et al. Avelumab, an anti-PD-L1 antibody, in patients with locally advanced or metastatic breast cancer: a phase 1b JAVELIN solid tumor study. *Breast Cancer Res. Treat.* **167**, 671–686 (2018).
- Esteva, F. J., Hubbard-Lucey, V. M., Tang, J. & Pusztai, L. Immunotherapy and targeted therapy combinations in metastatic breast cancer. *Lancet Oncol.* **20**, e175–e186 (2019).
- Zhang, J. et al. Immune-related biomarkers in triple-negative breast cancer. *Breast Cancer* **28**, 792–805 (2021).
- Wu, S. Z. et al. A single-cell and spatially resolved atlas of human breast cancers. *Nat. Genet.* **53**, 1334–1347 (2021).
- Miller, L. D. et al. Immunogenic subtypes of breast cancer delineated by gene classifiers of immune responsiveness. *Cancer Immunol. Res.* **4**, 600–610 (2016).
- Liu, Z., Li, M., Jiang, Z. & Wang, X. A comprehensive immunologic portrait of triple-negative breast cancer. *Transl. Oncol.* **11**, 311–329 (2018).
- O'Meara, T. A. & Tolaney, S. M. Tumor mutational burden as a predictor of immunotherapy response in breast cancer. *Oncotarget* **12**, 394–400 (2021).
- Huang, A. C. & Zappasodi, R. A decade of checkpoint blockade immunotherapy in melanoma: understanding the molecular basis for immune sensitivity and resistance. *Nat. Immunol.* **23**, 660–670 (2022).
- Bianchini, G., Balko, J. M., Mayer, I. A., Sanders, M. E. & Gianni, L. Triple-negative breast cancer: challenges and opportunities of a heterogeneous disease. *Nat. Rev. Clin. Oncol.* **13**, 674–690 (2016).
- Mao, Y. et al. The prognostic value of tumor-infiltrating lymphocytes in breast cancer: a systematic review and meta-analysis. *PLoS One* **11**, e0152500 (2016).
- Dieci, M. V. et al. Integration of tumour infiltrating lymphocytes, programmed cell-death ligand-1, CD8 and FOXP3 in prognostic models for triple-negative breast cancer: analysis of 244 stage I–III patients treated with standard therapy. *Eur. J. Cancer* **136**, 7–15 (2020).
- Huertas-Caro, C. A. et al. Tumor infiltrating lymphocytes (TILs) are a prognosis biomarker in Colombian patients with triple negative breast cancer. *Sci. Rep.* **13**, 21324 (2023).
- Galluzzi, L., Humeau, J., Buqué, A., Zitvogel, L. & Kroemer, G. Immunostimulation with chemotherapy in the era of immune checkpoint inhibitors. *Nat. Rev. Clin. Oncol.* **17**, 725–741 (2020).
- Pfirschke, C. et al. Immunogenic chemotherapy sensitizes tumors to checkpoint blockade therapy. *Immunity* **44**, 343–354 (2016).
- Schmid, P. et al. Atezolizumab and nab-paclitaxel in advanced triple-negative breast cancer. *N. Engl. J. Med.* **379**, 2108–2121 (2018).
- Zitvogel, L., Apetoh, L., Ghiringhelli, F. & Kroemer, G. Immunological aspects of cancer chemotherapy. *Nat. Rev. Immunol.* **8**, 59–73 (2008).
- Agostinetto, E., Gligorov, J. & Piccart, M. Systemic therapy for early-stage breast cancer: learning from the past to build the future. *Nat. Rev. Clin. Oncol.* **19**, 763–774 (2022).
- De Mattos-Arruda, L., Shen, R., Reis-Filho, J. S. & Cortés, J. Translating neoadjuvant therapy into survival benefits: one size does not fit all. *Nat. Rev. Clin. Oncol.* **13**, 566–579 (2016).
- Tufano, A. M., Teplinsky, E. & Landry, C. A. Updates in neoadjuvant therapy for triple negative breast cancer. *Clin. Breast Cancer* **21**, 1–9 (2021).
- Bernal-Estévez, D. A. et al. Autologous dendritic cells in combination with chemotherapy restore responsiveness of T cells in breast cancer patients: a single-arm phase I/II trial. *Front. Immunol.* **12**, 669965 (2021).
- Bernal-Estévez, D. A., García, O., Sánchez, R. & Parra-López, C. A. Monitoring the responsiveness of T and antigen presenting cell compartments in breast cancer patients is useful to predict clinical

- tumor response to neoadjuvant chemotherapy. *BMC Cancer* **18**, 77 (2018).
25. Cortes, J. et al. Pembrolizumab plus chemotherapy versus placebo plus chemotherapy for previously untreated locally recurrent inoperable or metastatic triple-negative breast cancer (KEYNOTE-355): a randomised, placebo-controlled, double-blind, phase 3 clinical trial. *Lancet* **396**, 1817–1828 (2020).
 26. Emens, L. A. et al. First-line atezolizumab plus nab-paclitaxel for unresectable, locally advanced, or metastatic triple-negative breast cancer: IMpassion130 final overall survival analysis. *Ann. Oncol.* **32**, 983–993 (2021).
 27. Chen, L. et al. Famitinib with camrelizumab and nab-paclitaxel for advanced immunomodulatory triple-negative breast cancer (FUTURE-C-Plus): an open-label, single-arm, phase II trial. *Clin. Cancer Res.* **28**, 2807–2817 (2022).
 28. Munzone, E. & Colleoni, M. Clinical overview of metronomic chemotherapy in breast cancer. *Nat. Rev. Clin. Oncol.* **12**, 631–644 (2015).
 29. Mathios, D. et al. Anti-PD-1 antitumor immunity is enhanced by local and abrogated by systemic chemotherapy in GBM. *Sci. Transl. Med.* **8**, 370ra180 (2016).
 30. Ménétrier-Caux, C., Ray-Coquard, I., Blay, J.-Y. & Caux, C. Lymphopenia in cancer patients and its effects on response to immunotherapy: an opportunity for combination with cytokines? *J. Immunother. Cancer* **7**, 85 (2019).
 31. Li, L., Zhang, F., Liu, Z. & Fan, Z. Immunotherapy for triple-negative breast cancer: combination strategies to improve outcome. *Cancers (Basel)* **15**, 321–348 (2023).
 32. Zhong, L. et al. Small molecules in targeted cancer therapy: advances, challenges, and future perspectives. *Sig. Transduct. Target. Ther.* **6**, 201–248 (2021).
 33. Min, H.-Y. & Lee, H.-Y. Molecular targeted therapy for anticancer treatment. *Exp. Mol. Med.* **54**, 1670–1694 (2022).
 34. Fassl, A., Geng, Y. & Sicsinski, P. CDK4 and CDK6 kinases: from basic science to cancer therapy. *Science* **375**, eabc1495 (2022).
 35. Hafner, M. et al. Multiomics profiling establishes the polypharmacology of FDA-approved CDK4/6 inhibitors and the potential for differential clinical activity. *Cell Chem. Biol.* **26**, 1067–1080 (2019).
 36. Chong, Q.-Y. et al. A unique CDK4/6 inhibitor: current and future therapeutic strategies of abemaciclib. *Pharmacol. Res.* **156**, 104686 (2020).
 37. Wells, A. D. & Morawski, P. A. New roles for cyclin-dependent kinases in T cell biology: linking cell division and differentiation. *Nat. Rev. Immunol.* **14**, 261–270 (2014).
 38. Kim, E. S. Abemaciclib: first global approval. *Drugs* **77**, 2063–2070 (2017).
 39. Deng, J. et al. CDK4/6 inhibition augments antitumor immunity by enhancing T-cell activation. *Cancer Discov.* **8**, 216–233 (2018).
 40. Álvarez-Fernández, M. & Malumbres, M. Mechanisms of sensitivity and resistance to CDK4/6 inhibition. *Cancer Cell* **37**, 514–529 (2020).
 41. Munn, D. H. & Mellor, A. L. IDO in the tumor microenvironment: inflammation, counter-regulation, and tolerance. *Trends Immunol.* **37**, 193–207 (2016).
 42. Labadie, B. W., Bao, R. & Luke, J. J. Reimagining IDO pathway inhibition in cancer immunotherapy via downstream focus on the tryptophan-kynurenine-aryl hydrocarbon axis. *Clin. Cancer Res.* **25**, 1462–1471 (2019).
 43. Le Naour, J., Galluzzi, L., Zitvogel, L., Kroemer, G. & Vacchelli, E. Trial watch: IDO inhibitors in cancer therapy. *Oncoimmunology* **9**, 1777625 (2020).
 44. Triplett, T. A. et al. Reversal of indoleamine 2,3-dioxygenase-mediated cancer immune suppression by systemic kynurenine depletion with a therapeutic enzyme. *Nat. Biotechnol.* **36**, 758–764 (2018).
 45. Zhu, M. M. T., Dancsok, A. R. & Nielsen, T. O. Indoleamine dioxygenase inhibitors: clinical rationale and current development. *Curr. Oncol. Rep.* **21**, 2 (2019).
 46. Jung, K. H. et al. Phase I study of the indoleamine 2,3-dioxygenase 1 (IDO1) inhibitor navoximod (GDC-0919) administered with PD-L1 inhibitor (Atezolizumab) in advanced solid tumors. *Clin. Cancer Res.* **25**, 3220–3228 (2019).
 47. Oliva, N., Conde, J., Wang, K. & Artzi, N. Designing hydrogels for on-demand therapy. *Acc. Chem. Res.* **50**, 669–679 (2017).
 48. Askari, E. et al. Stimuli-responsive hydrogels for local post-surgical drug delivery. *Gels* **6**, 14–44 (2020).
 49. Xie, C. et al. Synthesis and properties of injectable hydrogel for tissue filling. *Pharmaceutics* **16**, 430–453 (2024).
 50. Wang, F. et al. Tumour sensitization via the extended intratumoural release of a STING agonist and camptothecin from a self-assembled hydrogel. *Nat. Biomed. Eng.* **4**, 1090–1101 (2020).
 51. Majumder, P. et al. Surface-fill hydrogel attenuates the oncogenic signature of complex anatomical surface cancer in a single application. *Nat. Nanotechnol.* **16**, 1251–1259 (2021).
 52. Li, J. & Mooney, D. J. Designing hydrogels for controlled drug delivery. *Nat. Rev. Mater.* **1**, 16071 (2016).
 53. Su, H. et al. Recent progress in exploiting small molecule peptides as supramolecular hydrogelators. *Chin. J. Polym. Sci.* **35**, 1194–1211 (2017).
 54. Schiapparelli, P. et al. Self-assembling and self-formulating pro-drug hydrogelator extends survival in a glioblastoma resection and recurrence model. *J. Control. Release* **319**, 311–321 (2020).
 55. Chakraborty, R. W. et al. Fine-tuning the linear release rate of paclitaxel-bearing supramolecular filament hydrogels through molecular engineering. *ACS Nano* **13**, 7780–7790 (2019).
 56. Cai, Y. et al. Recent progress in the design and application of supramolecular peptide hydrogels in cancer therapy. *Adv. Healthc. Mater.* **10**, e2001239 (2021).
 57. Hu, C. et al. Regulating cancer associated fibroblasts with losartan-loaded injectable peptide hydrogel to potentiate chemotherapy in inhibiting growth and lung metastasis of triple negative breast cancer. *Biomaterials* **144**, 60–72 (2017).
 58. Zhao, X. et al. Injectable peptide hydrogel as intraperitoneal triptolide depot for the treatment of orthotopic hepatocellular carcinoma. *Acta Pharm. Sin. B* **9**, 1050–1060 (2019).
 59. Morrison, L., Loibl, S. & Turner, N. C. The CDK4/6 inhibitor revolution — a game-changing era for breast cancer treatment. *Nat. Rev. Clin. Oncol.* **21**, 89–105 (2024).
 60. Schrörs, B. et al. Multi-omics characterization of the 4T1 murine mammary gland tumor model. *Front. Oncol.* **10**, 1195 (2020).
 61. Wang, J. et al. High-density lipoprotein modulates tumor-associated macrophage for chemoimmunotherapy of hepatocellular carcinoma. *Nano Today* **37**, 101064 (2021).
 62. Fan, H. et al. DNA damage induced by CDK4 and CDK6 blockade triggers anti-tumor immune responses through cGAS-STING pathway. *Commun. Biol.* **6**, 1041 (2023).
 63. Zitvogel, L., Galluzzi, L., Kepp, O., Smyth, M. J. & Kroemer, G. Type I interferons in anticancer immunity. *Nat. Rev. Immunol.* **15**, 405–414 (2015).
 64. McNab, F., Mayer-Barber, K., Sher, A., Wack, A. & O’Garra, A. Type I interferons in infectious disease. *Nat. Rev. Immunol.* **15**, 87–103 (2015).
 65. Zhai, Y. et al. T lymphocyte membrane-decorated epigenetic nanoinducer of interferons for cancer immunotherapy. *Nat. Nanotechnol.* **16**, 1271–1280 (2021).
 66. Schmid, P. et al. VP7-2021: KEYNOTE-522: phase III study of neoadjuvant pembrolizumab + chemotherapy vs. placebo + chemotherapy, followed by adjuvant pembrolizumab vs. placebo for early-stage TNBC. *Ann. Oncol.* **32**, 1198–1200 (2021).

67. Wang, X. et al. Spatial predictors of immunotherapy response in triple-negative breast cancer. *Nature* **621**, 868–876 (2023).
68. Yan, C. et al. Injectable solid hydrogel: mechanism of shear-thinning and immediate recovery of injectable β -hairpin peptide hydrogels. *Soft Matter* **6**, 5143–5156 (2010).
69. Salvador-Coloma, C. et al. Immunosuppressive profiles in liquid biopsy at diagnosis predict response to neoadjuvant chemotherapy in triple-negative breast cancer. *Eur. J. Cancer* **139**, 119–134 (2020).
70. Offringa, R., Kötznér, L., Huck, B. & Urbahns, K. The expanding role for small molecules in immuno-oncology. *Nat. Rev. Drug Discov.* **21**, 821–840 (2022).

Acknowledgements

This work was supported by the National Key R&D Program of China (2022YFC3401400 to Y.L.), National Natural Science Foundation of China (32171374 and 32371457 to P.Z.), Chinese Academy of Sciences (Y2021076 to P.Z., 153631KYSB20190013 to Y.L.), National Natural Science Foundation of Shandong Province (ZR2019ZD25 to Y.L.) and Shandong Laboratory Program (SYS202205 to Y.L.). We thank the staff members of the Integrated Laser Microscope System at the National Facility for Protein Science in Shanghai (NFPS), Shanghai Advanced Research Institute, Chinese Academy of Sciences, China for sample preparation, data collection and analysis. We acknowledge the help given to us by Prof. Bin Zhang and Yaguang Lu for the characterization of the hydrogels.

Author contributions

B.Z., Y.C., and P.Z. conceived the project and designed all the experiments; B.Z. and Y.C. performed the synthesis of the conjugate and the characterization of the hydrogel system; L.Zhao performed the evaluation of the rheological properties of hydrogels; B.Z. and Y.C. contributed to the cell experiments in vitro; Q.Y. and H.Z. contributed to the construction of indicated cell lines; B.Z., Y.C., L.Zhou, J.C., X.Shan, X.Sun, X.G., and W.Z. performed the animal experiments and analyzed the data; B.Z., Y.C., and P.Z. wrote the original manuscript; P.Z. and Y.L. revised the manuscript; all authors discussed the results and edited the manuscript; P.Z. and Y.L. supervised the project.

Competing interests

The authors declare that they have no competing interests.

Additional information

Supplementary information The online version contains supplementary material available at <https://doi.org/10.1038/s41467-025-55904-z>.

Correspondence and requests for materials should be addressed to Pengcheng Zhang or Yaping Li.

Peer review information *Nature Communications* thanks Xiongbing Zu, Paola Zagami and the other, anonymous, reviewer(s) for their contribution to the peer review of this work. A peer review file is available.

Reprints and permissions information is available at <http://www.nature.com/reprints>

Publisher's note Springer Nature remains neutral with regard to jurisdictional claims in published maps and institutional affiliations.

Open Access This article is licensed under a Creative Commons Attribution-NonCommercial-NoDerivatives 4.0 International License, which permits any non-commercial use, sharing, distribution and reproduction in any medium or format, as long as you give appropriate credit to the original author(s) and the source, provide a link to the Creative Commons licence, and indicate if you modified the licensed material. You do not have permission under this licence to share adapted material derived from this article or parts of it. The images or other third party material in this article are included in the article's Creative Commons licence, unless indicated otherwise in a credit line to the material. If material is not included in the article's Creative Commons licence and your intended use is not permitted by statutory regulation or exceeds the permitted use, you will need to obtain permission directly from the copyright holder. To view a copy of this licence, visit <http://creativecommons.org/licenses/by-nc-nd/4.0/>.

© The Author(s) 2025

¹State Key Laboratory of Drug Research & Center of Pharmaceutics, Shanghai Institute of Materia Medica, Chinese Academy of Sciences, Shanghai, China. ²University of Chinese Academy of Sciences, No.19A Yuquan Road, Beijing, China. ³Yantai Key Laboratory of Nanomedicine & Advanced Preparations, Yantai Institute of Pharmaceutical Science, Shandong, China. ⁴School of Chinese Materia Medica, Nanjing University of Chinese Medicine, Nanjing, China. ⁵School of Chemical Engineering, Zhengzhou University, Zhengzhou, China. ⁶State Key Laboratory of Oncogenes and Related Genes, Renji-Med-X Stem Cell Research Center, Department of Urology, Ren Ji Hospital, School of Medicine and School of Biomedical Engineering, Shanghai Jiao Tong University, Shanghai, China. ⁷National Advanced Medical Engineering Research Center, China State Institute of Pharmaceutical Industry, Shanghai, China. ⁸School of Biomedical Engineering & State Key Laboratory of Advanced Medical Materials and Devices, ShanghaiTech University, Shanghai, China. ⁹Shandong Laboratory of Yantai Drug Discovery, Bohai rim Advanced Research Institute for Drug Discovery, Shandong, China. ¹⁰These authors contributed equally: Binyu Zhu, Ying Cai.

✉ e-mail: zhangpch1@shanghaitech.edu.cn; ypli@simm.ac.cn